Imaging breast cancer using a dual-ligand nanochain particle

Gil Covarrubias[1], Anthony Cha[1], Abdelrahman Rahmy[1], Morgan Lorkowski[1], Vindya Perera[1], Bernadette O. Erokwu[2,3], Chris Flask[2,3,4], Pubudu M. Peiris[1], William P. Schiemann[4], Efstathios Karathanasis[1,2,3,4]

[1] Department of Biomedical Engineering, Case Western Reserve University, Cleveland, Ohio

[2] Department of Radiology, Case Western Reserve University, Cleveland, Ohio

[3] Case Center for Imaging Research, Case Western Reserve University, Cleveland, Ohio

[4] Case Comprehensive Cancer Center, Case Western Reserve University, Cleveland, Ohio

Author to whom correspondence should be addressed: Efstathios Karathanasis

2071 Martin Luther King Jr. Drive, Wickenden Building, Cleveland, Ohio 44106, USA

Phone: +1-216-844-5281; Fax: +1-216-844-4987; Email: stathis@case.edu

ABSTRACT

Nanoparticles often only exploit the upregulation of a receptor on cancer cells to enhance intratumoral deposition of therapeutic and imaging agents. However, a single targeting moiety assumes that a tumor is homogenous and static. Tumoral microenvironments are both heterogenous and dynamic, often displaying variable spatial and temporal expression of targetable receptors throughout disease progression. Here, we evaluated the *in vivo* performance of an iron oxide nanoparticle in terms of targeting and imaging of orthotropic mouse models of aggressive breast tumors. The nanoparticle, a multi-component nanochain, was comprised of 3-5 iron oxide nanoparticles chemically linked in a linear chain. The nanoparticle's surface was decorated with two types of ligands each targeting two different upregulated biomarkers on the tumor endothelium, P-selectin and fibronectin. The nanochain exhibited improved tumor deposition not only through vascular targeting but also through its elongated structure. A single-ligand nanochain exhibited a ~2.5-fold higher intratumoral deposition than a spherical nanoparticle variant. Furthermore, the dual-ligand nanochain exhibited higher consistency in generating detectable MR signals compared to a single-ligand nanochain. Using a 7T MRI, the dual-ligand nanochains exhibited highly detectable MR signal within 3h after injection in two different animal models of breast cancer.

KEYWORDS

Iron oxide nanochains; dual-ligand nanoparticle; breast cancer, MRI

51

52

53

INTRODUCTION

55   Imaging is critical for management of patients with breast cancer including diagnosis,

56   treatment planning and response assessments. To improve cancer imaging, various targeting

57   schemes have been employed to direct nanoparticle imaging agents to cancers [1, 2]. Traditional

58   targeting strategies decorate the surface of nanoparticles with a ligand directing them to

59   upregulated receptors on breast cancer cells within the tumor interstitium. Rather than targeting

60   the tumor interstitium, an alternative strategy is to use vascular targeting and direct the

61   nanoparticles to the altered endothelium associated with breast cancer. The endothelium of

62   tumors, including those of the breast, displays a wide variety of targetable biomarkers that are not

63   readily found on healthy endothelium. For circulating nanoparticles, the endothelium is the closest

64   point-of-contact, which facilitates direct access to the targetable vascular biomarkers of the

65   disease [3-9]. Considering their size and multivalent avidity, nanoparticles are ideal for vascular

66   targeting.

67   Further, the shape of the nanoparticle can dictate its targeting avidity [7, 10-12]. Recently,

68   we reported a new one-pot synthetic concept for making multicomponent chain-like nanoparticles

69   (termed nanochains), which are comprised of about three iron oxide nanospheres chemically

70   linked into a linear, chain-like assembly [13]. The chain-like shape of the nanoparticles facilitates

71   geometrically enhanced multivalent attachment on vascular targets, resulting in rapid and

72   effective deposition of the nanochains onto the endothelium of tumors [5, 8, 13, 14].

73   In addition to adjusting the shape of nanoparticles, they can also be decorated with more

74   than one type of targeting ligand [3, 15]. This provides great flexibility in the particle's design

75   allowing targeted nanoparticles to consider the dynamic nature of tumors. As cancer cells evolve,

76   the surrounding vascular reflects this behavior by having continual changes in the expression of

77 targetable biomarkers both spatially and temporally [16-22]. In previous work [3, 6], we have

78 shown that a multi-ligand nanoparticle with two or more types of ligands can account for the

79 spatiotemporal alterations in the expression patterns of targetable receptors on the endothelium

80 of tumors, which are missed by single-ligand nanoparticles.

81 Here, we evaluated the performance of a dual-ligand nanochain as a targeted MR imaging

82 agent and its ability to target breast cancer. We employed two different peptides as ligands on

83 the nanoparticles that target 1) a vascular receptor on the remodeled endothelium of tumors (P-

84 selectin) [23-33], and 2) an extracellular biomarker in the near-perivascular regions of tumors

85 (fibronectin) [34-37]. It should be noted that the tumor endothelium often acts as a mirror reflecting

86 various cancerous activities of the tumor interstitium. Overexpression of P-selectin is linked with

87 angiogenesis and is prominent on proliferating endothelial cells. On the other hand, abundance

88 of fibronectin in the perivascular regions of tumors is strongly associated with migration and

89 invasion of cancer cells. Considering their insignificant expression on the endothelium of healthy

90 tissues, these biomarkers are an ideal fit to a vascular targeting scheme. Using a mouse

91 syngeneic model of triple-negative breast cancer, we compared the vascular targeting abilities of

92 the dual-ligand nanochain to a single-ligand nanochain variant and its spherical counterpart.

93 Overall, we show that the combination of two different ligands on the nanochain particle effectively

94 captures the dynamic nature of breast cancers and targets the spatial and temporal variations in

95 receptor presentation on the tumor endothelium.

96 **MATERIALS AND METHODS**

97 **Synthesis of Parent Iron Oxide Nanoparticles**

98 Iron oxide nanoparticles are synthesized using a co-precipitation method of Fe(II) and

99 Fe(III) ions. Briefly, a 2 to 1 molar ratio of $FeCl_3.6H_2O$ and $FeCl_2.4H_2O$ was dissolved in a 5mL

100 solution of deoxygenated water. To the iron chloride solution, 5mL of a 0.4M HCl solution was

101 added and allowed to stir vigorously. The iron precursor solution was then added to a 50mL

102 solution of 0.5M NaOH at 80°C under a constant flow of nitrogen. The reaction continued for an

103   additional 15 minutes with stirring. Upon placing the iron precursor solution in the preheated

104   NaOH solution, the reaction mixture immediately turned black indicating the formation of iron

105   oxide nanoparticles. Using magnetic separation, the iron oxide solution was cleaned using

106   deoxygenated water until a stable ferrofluid was developed. Once a stable ferrofluid was obtained,

107   the particle volume was increased to a total volume of 50mL using deoxygenated water. In order

108   to prevent the aggregation of iron oxide nanoparticles, 340 mg of anhydrous citric acid was added

109   to the particle solution and the pH was consequentially increased to 5.2 using ammonia. This

110   reaction was heated for 2 hours under a constant flow of nitrogen at 80°C. After the reaction was

111   completed large and unreacted particles were removed using multiple centrifugation steps at 5000

112   rpm in 30-minute increments. Excess citric acid was removed using Amicon® Ultra-15 centrifugal

113   filters.

114   The surface of the iron oxide particle was modified using silane-PEG-NH_2 or silane-PEG-

115   COOH (2000kDa). Citric coated iron oxide nanoparticles were concentrated to 1mg/mL in Milli-Q

116   water and the pH was adjusted to 11 using ammonia. 10 mg of silane-PEG-NH_2 was added to

117   citric coated iron oxides and allowed to react for 24 hours while shaking. The reaction was taken

118   to completion by heating the nanoparticle solution to 80°C for 2 hours in order to achieve covalent

119   linking between the iron oxide surface and the polymer. The resultant PEGylated nanoparticles

120   (Fe_3O_4@silane-PEG-COOh or NH_2), were concentrated using Amicon® Ultra-15 centrifugal

121   filters. The concentrated IONP-NH_2 solution was stored at 4°C.

122   Fluorescent labelling was used to determine the total amount of functional groups on the

123   surface of the iron oxide nanoparticles. To assess the quantity of amine functional groups, a 10-

124   molar excess of Alexa Fluor® 488 NHS ester (Invitrogen, Carlsbad, CA) was added to the IONP-

125   NH_2 particles and allowed to react for 2 hours in the dark. The excess fluorophore was dialyzed

126   out in PBS using a 100,000 Da MW cut-off membrane bag. All fluorescent measurements were

127   performed on a fluorescent plate reader (Synergy HT; BioTek Instruments, Winooski, VT) using

128   a 480nm excitation and a 520 emission. The fluorescent intensity of the nanoparticles was

129   compared to a standard curve. Iron content was measured using ICP-OES after sample digestion

130   in a 1 to 4 volumetric ratio of concentrated HNO_3 to concentrated HCl. Iron oxide nanoparticle

131   calculations were performed assuming only Fe_3O_4 particles were made and with a 5.2 g/cm^3

132   density.

Synthesis of Chain-like Nanoparticles

134   First, the parent nanoparticles (IONP-COOH and $IONP-NH_2$) were transferred from water

135   to dimethylformamide (DMF) and heated to evaporate all water. The concentration of the

136   nanoparticles was then adjusted to 1 mg/mL Fe. The carboxyl groups on the IONP-COOH

137   nanoparticles were activated with an excess of *N,N'*-Dicyclohexylcarbodiimide over the available

138   COOH groups in the presence of pyridine.

139    $IONP-NH_2$ nanoparticles and the activated IONP-COOH were mixed at a ratio of 2.5:1 and

140   allowed to react for 30 min. The reaction was then arrested by 'deactivating' the carboxyl groups

141   using a 10-molar excess of ethylenediamine (relative to the number of carboxyl groups). Finally,

142   nanochains were transferred to water and were separated by centrifugation with Amicon® Ultra-

143   15 centrifugal filters. To further clean nanochains from any unreacted parent nanoparticles, a

144   strong magnet was used.

Functionalization of Nanoparticles with Targeting Ligands

146   Functionalization of nanoparticles with vascular targeting ligands was accomplished via a

147   sulfo-SMCC crosslinker. The nanoparticle composites, $IONP-NH_2$ and $NC-NH_2$, had terminal

148   amine groups that are readily available for conjugation with available thiol groups on the cysteine

149   end of the targeting ligands. Here P-selectin-targeting peptide CDAEWVDVS and fibrin-targeting

150   peptide CREKA were used. Briefly, sulfo-SMCC contains two functional terminal groups on

151   contralateral sides; an amine-reactive N-hydroxysuccinimide (NHS ester) and a sulfhydryl-

152   reactive maleimide group. First, sulfo-SMCC in a 2-molar excess to available amine groups on

153   the $IONP-NH_2$ solution and allowed to react for 30 minutes while shaking. Next, a 2:3 molar excess

154   of sulfo-SMCC to targeting ligand was added and allowed to react for an additional 2 hours while

155   shaking. The functionalized product was dialyzed against PBS using a 100,000 Da MW cut-off

156   dialysis bag to remove excess peptide and crosslinker. For dual-ligand functionalization equal

157   molar peptides were added with the overall molar excess to sulfo-SMCC still at a 2:3 molar ratio

158   (2-moles sulfo-SMCC:1.5 moles fibrin-targeting peptide:1.5 moles P-selectin targeting peptide).

159   Bio-Rad DC protein assay was used to quantify the total number of conjugated peptides.

160   Here, 200 µL of Bio-Rad dye solution (1 to 2 parts Bio-Rad dye and water) was added to an 800

161   µL solution of 10 mg/mL particles and vortexed. The absorbance of the sample was obtained at

162   595 nm after incubating the sample for 15 minutes. The absorbance value was compared to a

163   standard curve, which was obtained by measuring the known absorbance of known

164   concentrations of CREKA, P-selectin peptide or both.

Murine Tumor Models

166   All animal procedures were conducted under a protocol approved by the Institutional

167   Animal Care and Use Committee (IACUC) at Case Western Reserve University. The well-being

168   of the animals took priority over continuation of planned interventions. All animals received

169   standard care, including *ad libitum* access to food and water, a 12/12 light/dark cycle, appropriate

170   temperature and humidity. All animals received standard care ensuring proper protocol guidelines

171   were followed.

172   We used two different mammary fat pad models developed from 4T1 and D2.A1 cancer

173   cell lines. Both cell lines were transfected with both a luciferase and a green fluorescent protein

174   (GFP) encoding lentivirus. 4T1 and D2.A1 mammary fat pad inoculations were preformed per

175   approved institutional protocol. Briefly, 0.5×10^6 4T1-Luc-GFP cells were orthotopically inoculated

176   in the right 9th inguinal gland of female BALB/cJ mice while anesthetized using an isoflurane

177   inhalant. Using a previously established timeline, mice studies were preformed approximately 10-

178   14 days post 4T1 inoculations until bioluminescent signals reached $1\text{-}2 \times 10^8$ photons/sec. D2.A1

179   studies were performed on a similar timeline. The animals were closely monitored on a daily basis

180   to ensure they did not suffer adverse effects resulting from tumor inoculations.

181   The well-being of the animals took priority over precise measurements in decisions

182   regarding euthanasia or other interventions. All procedures were conducted using anesthetic to

183   minimize pain and distress. The inhalant anesthetic, isoflurane, was used as the primary

184   anesthesia in our experiments. However, developing tumors may ultimately result in some level

185   of distress or discomfort in these mice. If, during the time following tumor inoculation the animal

186   showed signs of post-procedure pain, the animal was euthanized. The research team, as well as

187   the veterinary team of the animal facility, diligently monitored the condition of the animals, and

188   removed any animal exhibiting signs of pain or distress as soon as humanly possible. When an

189   animal showed distress or stopped eating and drinking (visually evaluated or there was a 15%

190   loss of body weight), the animal was immediately euthanized. If it was observed that the tumor

191   became 10% of the body mass of the animal or if there were changes in grooming, weight,

192   behaviors, or kyphosis, the animal were immediately euthanized. Additionally, if we observed that

193   an animal was suffering from inactivity, prostration, labored breathing, sunken eyes, hunched

194   posture, piloerection/matted fur, unresolving skin ulcers, abnormal vocalization when handled,

195   emaciation or anorexia, the animal was immediately euthanized. In all cases euthanasia was

196   carried out in a CO_2 chamber.

197   **Bioluminescent and *Ex Vivo* Fluorescent Imaging**

198   Using the IVIS Spectrum system, bioluminescent imaging (BLI) was performed 10 minutes

199   after an intraperitoneal injection of 200 µL of a 12.5 mg/mL solution of D-luciferin in sterile PBS.

200   A BLI was taken every 3 days until the terminal point of the study. At the terminal point of the

201   study, tumors were resected and used for *ex vivo* GFP fluorescent imaging, *ex vivo* tissue

202   relaxivity or histological analysis.

203   **Histological Analysis**

204   Immunohistochemistry was performed to determine the topological distribution of

205   available targeting sites for the ligands of interest, fibrin-associated proteins and P-selectin. Mice

206   were anesthetized with an intraperitoneal injection of ketamine/xylazine and transcardially

207   perfused with heparinized PBS followed by 4% paraformaldehyde in PBS. Mammary tumor

208   tissues were resected and placed in 4% paraformaldehyde for 24 hours. Tumor tissues were

209   washed 3 times in PBS and placed in a 30% sucrose (w/v) for 48 hours. Finally, the tumor tissues

210   were placed in OCT and stored at -80°C for two days prior to cryosectioning. Subsequent tissue

211   sections were sliced at 12 μm and used for histological staining. To identify the location of

212   fibronectin, P-selectin and the tumor microvasculature immunohistochemistry staining was

213   performed using anti-fibrin and anti-P-selectin primary antibodies for each of the ligands of interest

214   and an endothelial antigen CD31 for the vasculature. A secondary antibody tagged with Alexa

215   Fluor® 568 was added to do fluorescent imaging on the stained tissue sections. The tissue

216   sections were counterstained using a DAPI nuclear stain. Tumor cells were imaged with their GFP

217   tagged marker. The tissue sections were imaged at 5x, 10x and 20x using a Zeiss Axio Observer

218   Z1 motorized inverted fluorescent microscope. For larger sized montages, the Axio Vision

219   software automatic tiling was achieved using the Mosaic acquisition feature. Nanochain particles

220   were detected using a Prussian Blue stain and imaged using brightfield.

221   *Ex Vivo* **Tissue Relaxivity**

222   The *ex vivo* tissue relaxivity was calculated using a 1.5 T Bruker Minispec mq60. Mice

223   were anesthetized with an intraperitoneal injection of ketamine/xylazine and transcardially

224   perfused with heparinized PBS. Kidneys, liver, spleen, lungs and tumors were excised and

225   grinded in 1 mL of water. Grounded tissues were placed in 5mm disposable grade NMR tubes.

226   Samples were placed in the 1.5 T Bruker Minispec and relaxation values were recorded for use

227   in the analysis of tissue relaxivity per mass of collected tissue.

228   **MR imaging**

229   MR images were acquired using a 7 T Bruker MRI system. A volume coil (3.5 cm inner

230   diameter) was employed. The sequence used was a Rapid Acquisition with Relaxation

231   Enhancement (RARE). High-resolution images were obtained before and 3 hours after IV injection

232   of the nanochains (at a dose of 10 mg Fe per kg b.w.) using a T_2-weighted RARE sequence with

233   the following parameters: TR/TE = 3646.6/31 ms, matrix = 256 × 256, FOV = 3 × 3 cm, and 5

234   averages. The acquisition time approximately 10 minutes using a gating acquisition method. This

235   resulted in an in-plane spatial resolution of 111.7 μm and a slice thickness of 1 mm.

236   **Statistical Analysis**

237   Statistics were performed in Prism version 7 for Mac (GraphPad Software, La Jolla, CA,

238   USA). All the experiments were performed in triplicates unless stated otherwise. Data are

239   represented as mean ± s.d. In cases where data met the assumptions necessary for parametric

240   statistics, analysis of differences between two groups was performed using two-tailed Student's t-

241   test assuming equal variance. Data from three or more groups were analyzed with a one-way

242   analysis of variance (ANOVA) that was corrected for multiple comparisons using the Holm−Sidak

243   method.

244   To determine the detection accuracy of particle conjugates z-score probabilities values

245   were obtained to evaluate the effective belonginess of a single particle conjugate member to a

246   healthy mammary fat pad population. The z-score probabilities were obtained via a confidence

247   interval of 90% (α was set to 0.1). If a population member fell inside of the 90% confidence interval

248   it was considered to be part of the healthy mammary fat pad population; these members were

249   considered to be false negatives as the tumors were present however the p-values indicated they

250   fell in the healthy population.

251   **RESULTS**

252   **Nanoparticle Fabrication**

253   We recently developed a new simple 'one-pot' synthetic concept for making iron oxide

254   nanochains with high yield and consistency [13]. Fig 1a shows an illustration of the nanochain

255   particles. Briefly, the one-pot synthesis utilized two types of the parent iron oxide nanoparticle

256   (IONP) based on the functional group on the particle's surface (Fig 1b). The IONP were decorated

257   with either PEG-amine (NP-NH$_2$) or PEG-carboxyl (NP-COOH). First, the carboxyl groups on the

258   NP-COOH particles were activated with DCC. To avoid hydrolysis of the activated COOH

259   intermediate, the one-pot synthesis was performed in an organic solvent (*i.e.*, absence of water).

260   Once activated NP-COOH and NP-NH$_2$ were mixed, the nanoparticles started reacting with each

261   other. The reaction rate and size of the agglomerates can be dictated by the stirring rate,

262   stoichiometry and concentration of the starting IONP particles. By mixing NP-NH$_2$ and NP-COOH

263   at a ratio of ~2:1, two NP-NH$_2$ particles were initially linked with one 'activated' NP-COOH forming

264   a trimeric nanochain. We identified the optimal reaction time and parameters that generated well-

265   defined short nanochains and not large agglomerates. Using dynamic light scattering, longitudinal

266   measurement of the hydrodynamic size of the reaction mixture indicated the progression and

267   growth of the nanochain. Fig 1c shows that the two populations of the starting parent IONP with

268   sizes of 21 and 33 nm disappeared, while the nanochains appeared in a new population with the

269   mean size being ~80 nm. The size and structure of the nanochains was confirmed in TEM images

270   (Fig 1d). The iron concentration was measured using ICP-OES, which was used in all the *in vivo*

271   studies to accurately calculate the dose of the agents that was injected into the animals. Based

272   on previous work [13], we also quantified the number of primary amines on the surface of

273   nanochains using fluorescence labelling. To determine the number of surface amines, an excess

274   of Alexa Fluor® 488 NHS ester reacted with the nanoparticles for 2h followed by extensive dialysis

275   to remove unbound fluorophore. Fluorescence measurements showed that the nanochain

276   exhibited about 700 amines per particle. The fibronectin-targeting peptide (CREKA) and P-

277   selectin-targeting peptide CDAEWVDVS were effectively conjugated onto the available amines

278   on the surface of the nanochains using the heterobifunctional crosslinker sulfo-SMCC. Using

279   HPLC assays, the number of peptides was quantified confirming that the single-ligand nanochains

280   displayed ~700 peptides per particle, whereas the dual-ligand variant had the available amines

281   split approximately in half for each peptide. More details on the synthesis and characterization of

282   the nanochains can be found in a previous publication [13].

283

284 *Fig 1. Synthesis and characterization of the nanochain particles. (a) Illustration shows the dual-*

285 *ligand nanochain particle. (b) Reaction scheme shows the synthesis of nanochains using parent*

286 *iron oxide nanoparticles with different surface functionality. (c) The size of the parent*

287 *nanoparticles and nanochains was measured using dynamic light scattering (DLS). (d) TEM*

288 *image of nanochain particles is shown. (e) The transverse (R2) relaxivity of the nanochains was*

289 *measured at 1.5 Tesla using a relaxometer.*

290

291 **Organ distribution**

292   We evaluated the biodistribution of the dual-ligand nanochains in the liver, spleen, lungs

293 and kidneys of mice 3 h after systemic administration *via* tail vein injection. The 3-hour time point

294 was selected based on the timeframe of vascular targeting of nanoparticles as explained in the

295 next section. The organ distribution of the dual-ligand nanochain was compared to a single-ligand

296 nanochain, the non-targeted nanochain variant, and the parent IONP with a single ligand. In

297 previous studies [13], the tissue deposition of targeted iron oxide nanoparticles was measured

298 using ICP-OES, which provided direct measurement of iron concentration in tissues using ICP.

299 However, the MR signal from tissues does not always correspond to the exact concentration of

300 the iron oxide particles in tissues. Iron oxide particles exhibit complex relaxation properties *in vivo*,

301 which is significantly influenced by iron clustering in the case of intracellular internalization of the

302 nanoparticles. Since the intended use of the dual-ligand nanochain is as an MR imaging agent,

303 we elected to measure the R2 relaxation rate in tissue as a surrogate metric of MR signal with

304 higher R2 value indicating stronger signal. Briefly, 3 h after injection of the nanoparticles, mice

305 were transcardially perfused with PBS and each organ was excised and homogenized. The

306 relaxation of samples of the homogenate was measured using a 1.5 T Bruker Minispec and was

307 recorded as tissue relaxivity per gram of tissue. This provided a robust method to measure

308 multiple samples in a convenient and quantitative manner. Fig 2 shows a comparison of the organ

309 distribution of the different nanoparticle variants. We tested dual-ligand nanochains targeting

310   fibronectin and P-selectin, non-targeted nanochains, single-ligand nanochains targeting P-

311   selectin, and single-ligand parent IONP targeting P-selectin. All the nanoparticles displayed

312   similar biodistribution patterns with the majority of the particles being cleared by the

313   reticuloendothelial organs (liver and spleen). The only difference was the higher clearance of the

314   spherical IONP from the spleen compared to all the nanochain formulations. This was in good

315   agreement with previous observations [5, 13, 38]. Further, the signal from the lungs and kidneys

316   was negligible for all formulations. These findings indicate that the use of one or two ligands did

317   not alter significantly the overall biodistribution patterns of the nanochains.

318

319   **Fig 2.** *Organ distribution of targeting variants of spherical or chain-like iron oxide nanoparticles.*

320   *Mice were systemically injected with nanoparticles at a dose of 10 mg/kg Fe. The dual-ligand*

321   *nanochain was compared to non-targeted nanochain, single-ligand nanochain targeting P-*

322   *selectin and single-ligand spherical nanoparticles targeting P-selectin (n=5 mice per formulation).*

323   *Animals were euthanized 3 h after injection and organs were extracted and homogenized. The*

324   *relaxation of the homogenate of different organs was measured using a 1.5 T Bruker Minispec*

325   *and was recorded as tissue relaxivity per gram of tissue.*

326

327   **Tumor targeting**

328   For these studies, we used the D2.A1 cancer cell line, which is a syngeneic mouse model

329   of triple-negative breast cancer. The D2.A1 cell line was engineered to stably express firefly

330   luciferase and green fluorescent protein (GFP). Using this cell line, we developed an orthotopic

331   D2.A1 model by inoculating the cancer cells into the mammary fat pad of BALB/c mice. Being a

332   very aggressive breast cancer, the typical survival of the animals is about 25 days. Bioluminescent

333   imaging was conducted ever 2-3 days post inoculation to monitor tumor growth. Animals were

334   selected for the targeting studies when bioluminescence signal of the tumor reached a value of

335   about 1.5×10^8 photons/s (approximately 2 weeks after tumor inoculation).

336   First, we compared the targeting performance of a single-ligand nanochain to its spherical

337   IONP counterpart. It should be noted that the spherical nanoparticles were the parent particles

338   used for the fabrication of the nanochains. Our previous studies showed that deposition of

339   targeted nanoparticles onto the endothelium of tumors is rapid and is maximized within 3 h after

340   systemic administration [3, 5, 6, 13]. Thus, we selected the 3-hour time point as the terminal point

341   when the tumors were perfused, excised, and homogenized. The relaxation of the tumor

342   homogenate was measured using a 1.5 T Bruker Minispec. As expected, when compared to

343   nanospheres, the nanochains favored tumor deposition due to geometrically enhanced targeting

344   of the tumor endothelium. Fig 3a shows that the single-ligand nanochains targeting P-selectin

345   exhibited about a 2.5-fold higher intratumoral deposition than their spherical counterpart. This is

346   in good agreement with a previous study that showed that nanochains facilitated superior vascular

347   targeting of brain tumors than spherical nanoparticles [13]. We then compared a single-ligand

348   nanochain to the dual-ligand nanochain. In a previous study, we showed that P-selecting-targeting

349   nanoparticles had similar intratumoral deposition to fibronectin-targeting nanoparticles [6]. Thus,

350   we tested only one of the two possible single-ligand nanochain variants. As shown in Fig 3b, the

351   dual-ligand nanochains did not significantly outperform their single-ligand variants. However,

352   comparisons of the average values of each group often does not reveal the entire diagnostic

353   performance. For example, the single-ligand formulation could not consistently discriminate

354   cancerous tissues even though we carefully selected animals with similar tumor burdens (Fig 3c).

355   On the other hand, the dual-ligand formulation exhibited 100% success in separating tumor from

356   healthy mammary tissues (Fig 3d). In previous studies, we have observed a similar consistency

357   of targeting accuracy of multi-ligand nanoparticles in brain tumors [13] and metastasis [3].

358

359   *Fig 3. Comparison of tumor targeting accuracy of different targeted nanoparticles. (a) Single-*

360   *ligand nanochains targeting P-selectin and their spherical counterparts were IV injected in mice*

361   *bearing mammary D2.A1 tumors. All formulations were administered at the same dose (10 mg/kg*

362   *Fe). The animals were perfused 3 h after injection and the tumors were excised, homogenized*

363   *and measured using a 1.5 T Bruker Minispec (data are represented as mean ± s.d.; n=5 mice in*

364   *each group; unpaired t-test, P values: ****<0.0001). (b) The endogenous relaxation rate (R2) of*

365   *healthy mammary tissue were compared to those of tumor bearing mice after systemic injection*

366   *of single-ligand or dual-ligand nanochains (data are represented as mean ± s.d.; n=5 mice in each*

367   *group; unpaired t-test, P values: **<0.005). (c) Quantification of the bioluminescent signal*

368   *indicated similar tumor burden of the different groups of animals. (d) Z-score analysis was*

369   *performed to identify the belongingness of each tumor bearing mouse injected with a formulation*

370   *to a healthy mammary population. If the z-score probability value was larger than an alpha of*

371   *0.05, it signified that it was likely that the R2 value belonged to that of a healthy mammary tissue*

372   *as opposed to a diseased mammary.*

373

374   **Imaging of breast tumors using MRI**

375   The ability of the dual-ligand nanochain to image breast cancer was tested using a 7T

376   MRI. In addition to the orthotopic D2.A1 mouse model, we also used the orthotopic 4T1 mouse

377   model (n=3 for each tumor model). The 4T1 model is one of the standard models to study TNBC

378   development in immunocompetent mice. MR imaging was performed before and 3 h after tail-

379   vein injection of the dual-ligand nanochains at a dose of 10 mg/kg Fe. We used the same scanning

380   parameters in the pre- and post-injection images. The pre- and 3h post-injection images were

381   compared quantitatively by measuring the absolute MR signal intensity in the tumor and healthy

382   mammary fat pad. The signal intensity was normalized to the signal of the healthy mammary

383   tissue (scale: 0-1). A low value indicates high contrast in T2 images, whereas a value of 1

384   indicates no contrast compared to the pre-injection image. Fig 4a summarizes the measurements.

385   The pre-injection values of the tumors in the D2.A1 and 4T1 mouse models were close to 1

386   indicating negligible contrast compared to health mammary. On the other hand, injection of the

387   dual-ligand nanochains generated significant contrast enhancement in the tumors with a

388   normalized value of 0.82 and 0.59 for the 4T1 and D2.A1 tumors, respectively. Fig 4b shows

389   representative sagittal T2-weighted images before and 3 h after injection of the dual-ligand

390   nanochains in the D2.A1 mouse model.

391

392   *Fig 4. MR imaging of mice bearing mammary breast tumors using dual-ligand nanochains and a*

393   *7T MRI. (a) Animals with 4T1 or D2.A1 mammary tumors were imaged before and 3 h after tail*

394   *vein injection of dual-ligand nanochains at a dose of 10 mg/kg Fe. The signal intensity was*

395   *measured in the tumor and healthy mammary fat pad. The signal intensity normalized to the signal*

396   *of the healthy mammary tissue (scale: 0-1). The normalized values of 0 and 1 correspond to*

397   *maximum and minimum contrast, respectively, compared to the pre-injection values of healthy*

398   *mammary tissue (data are represented as mean ± s.d.; n=3 mice for each animal model; unpaired*

399   *t-test, P values: *<0.05, **<0.005). (b) Representative sagittal T2-weighted images of a mouse*

400   *bearing a D2.A1 mammary tumor before and 3 h after injection of dual-ligand nanochains.*

401

402

403   **Histological evaluation**

404   We performed histological analysis to confirm vascular targeting and deposition of the

405   dual-ligand nanochains in tumors. After the last MRI session, mice were intracardially perfused

406   with heparinized PBS. Tumors and normal mammary tissues were collected and processed for

407   histological evaluation. Direct fluorescence imaging of GFP (green) indicated the location of

408   breast cancer cells. The tissue slices were also immunohistochemically stained for the endothelial

409   antigen CD31, anti-fibronectin antibody and anti-P-selectin antibody. Using fluoresence

410   microscopy, Fig 5a shows representative images of the tumor indicating that the endothelium and

411   near-vascular regions exhibited overexpression of fibronectin and P-selectin. We should note that

412   negligible expression of fibronectin or P-selectin was observed on the endothelium in healthy

413   mammary tissues (images not shown). The associated expression of P-selectin and endothelium

414   with respect to tumor endothelium should favor vascular targeting of the dual-ligand nanochains.

415   In addition to fluorescence microscopy, bright-field microscopy was performed on the same

416   histological sections using the Prussian blue stain to visualize the iron oxide nanochains. Fig 5b

417   shows that dual-ligand nanochains were predominantly distributed around blood vessels in the

418   tumor.

419

420   **Fig 5.** *Histological evaluation of the expression of vascular biomarkers and intratumoral*

421   *deposition of targeted nanoparticles in the orthotopic D2.A1 mouse model. (a) Mice bearing*

422   *mammary D2.A1 tumors were euthanized 3 h after tail vein injection of dual-ligand nanochains at*

423   *a dose of 10 mg/kg iron. After perfusion, tumors were excised and processed for histology. Images*

424   *from serial tissue sections show that topology of fibronectin and P-selectin with respect to the*

425   *endothelium (10x magnification; nuclear stain: blue; cancer cells: green; CD31 endothelial marker*

426   *or fibronectin or P-selectin: red; overlay: yellow). (b) The near-perivascular deposition of the dual-*

427   *ligand nanochain was identified through an iron stain (left panel: 10x magnification; nuclear stain:*

428   *blue and CD31 endothelial marker: red; middle and right panels: 20x magnification; iron stain:*

429   *Prussian blue).*

430

431   **DISCUSSION**

432   Due to their size and multivalent avidity, nanoparticles are ideal for vascular targeting of

433   upregulated biomarkers on the tumor endothelium. Since the endothelium is the closest point-of-

434   contact, circulating nanoparticles in the bloodstream have direct access to scavenge the

435   endothelium for vascular biomarkers of cancer. Recently, we reported a new one-pot synthetic

436   concept for making multicomponent chain-like nanoparticles (termed nanochains), which are

437   comprised of about three iron oxide nanospheres chemically linked into a linear assembly [13].

438   Here we showed that targeting avidity can be dictated by adjusting the shape. Within 3 h post-

439   injection, vascular targeting of nanochains targeting P-selectin resulted in a 2.5-fold higher

440   deposition in breast tumors than targeting equivalent spherical nanoparticles.

441   Traditional targeting strategies use a single-ligand system that considers cancer as a

442   monolithic disease and fails to account for tumor heterogeneity. However, aggressive breast

443   tumors exhibit a dynamic tumor microenvironment with targetable vascular biomarkers being

444   continuously changing over time and space [39]. In this context, our previous studies showed

445   that vascular biomarkers often exhibited spatiotemporal variability, representing different stages

446   of tumor development [3]. Considering then that the altered endothelium associated with breast

447   cancer displays a diverse and dynamic set of targetable biomarkers. a combination of different

448   ligands on the same particle may be required to efficiently direct a nanoparticle to the majority of

449   a tumor volume.

450   In previous studies [3-9], we tested different peptides to direct nanoparticles to different

451   vascular biomarkers that represent various microenvironments of breast cancer, including $\alpha_v\beta_3$

452   integrin, P-selectin, EGFR, PTPμ, and fibronectin. In this work, we selected to target P-selectin

453   and fibronectin that represent different cancerous activities and stages of breast cancer

454   development. Upregulation of P-selectin is pronounced on proliferating endothelial cells and is

455   associated with the early response of cancer cells to hypoxia development and angiogenesis. On

456   the other hand, perivascular overexpression of fibronectin is critical in the migration and invasion

457   of cancer cells [34-37]. Not surprising, the dual-ligand nanochain variants exhibited significant

458   intratumoral deposition. We selected iron oxide as our nanomaterial basis due to its ability to

459   generate significant contrast in MR imaging. In two different animal models of breast cancer, MR

460   imaging and the dual-ligand nanochain facilitated precise detection of breast cancer. Taking under

461   consideration that diagnosis, treatment planning and response assessments of breast cancer rely

462   heavily on imaging, a more accurate imaging test for breast cancer can change patient

463   management by guiding early therapeutic interventions before the disease becomes

464   unmanageable.

CONCLUSIONS

The multicomponent nanochain represents a higher order nanostructure that is comprised of individual nanoparticles. By utilizing a simple 'one-pot' synthesis, nanochains were fabricated with high reproducibility, yield and consistency across batches. Further, the combination of two different ligands on the same nanochain particle effectively targeted the dynamic nature of breast tumors and generated highly detectable MR signals.

REFERENCES

1. Zhou Z, Lu ZR. Molecular imaging of the tumor microenvironment. Adv Drug Deliv Rev. 2017;113:24-48. Epub 2016/08/09. doi: 10.1016/j.addr.2016.07.012. PubMed PMID: 27497513.

2. Toy R, Bauer L, Hoimes C, Ghaghada KB, Karathanasis E. Targeted nanotechnology for cancer imaging. Adv Drug Deliv Rev. 2014;76:79-97. doi: 10.1016/j.addr.2014.08.002. PubMed PMID: 25116445; PubMed Central PMCID: PMC4169743.

488   3.   Doolittle E, Peiris PM, Doron G, Goldberg A, Tucci S, Rao S, et al. Spatiotemporal

489   Targeting of a Dual-Ligand Nanoparticle to Cancer Metastasis. ACS Nano.

490   2015;9(8):8012-21. doi: 10.1021/acsnano.5b01552. PubMed PMID: 26203676;

491   PubMed Central PMCID: PMC4579532.

492   4.   Toy R, Hayden E, Camann A, Berman Z, Vicente P, Tran E, et al. Multimodal in vivo

493   imaging exposes the voyage of nanoparticles in tumor microcirculation. ACS Nano.

494   2013;7(4):3118-29. doi: 10.1021/nn3053439. PubMed PMID: 23464827; PubMed

495   Central PMCID: PMC3640526.

496   5.   Peiris PM, Toy R, Doolittle E, Pansky J, Abramowski A, Tam M, et al. Imaging

497   metastasis using an integrin-targeting chain-shaped nanoparticle. ACS Nano.

498   2012;6(10):8783-95. doi: 10.1021/nn303833p. PubMed PMID: 23005348.

499   6.   Peiris PM, He F, Covarrubias G, Raghunathan S, Turan O, Lorkowski M, et al.

500   Precise targeting of cancer metastasis using multi-ligand nanoparticles incorporating

501   four different ligands. Nanoscale. 2018;10(15):6861-71. Epub 2018/04/06. doi:

502   10.1039/c8nr02513d. PubMed PMID: 29620124; PubMed Central PMCID:

503   PMCPMC5908762.

504   7.   Toy R, Peiris PM, Ghaghada KB, Karathanasis E. Shaping cancer nanomedicine:

505   the effect of particle shape on the in vivo journey of nanoparticles. Nanomedicine

506   (Lond). 2014;9(1):121-34. doi: 10.2217/nnm.13.191. PubMed PMID: 24354814.

507   8.   Peiris PM, Toy R, Abramowski A, Vicente P, Tucci S, Bauer L, et al. Treatment of

508   cancer micrometastasis using a multicomponent chain-like nanoparticle. J Control

509   Release. 2014;173:51-8. doi: 10.1016/j.jconrel.2013.10.031. PubMed PMID:

510   24188960.

511   9.   Peiris PM, Deb P, Doolittle E, Doron G, Goldberg A, Govender P, et al. Vascular

512   Targeting of a Gold Nanoparticle to Breast Cancer Metastasis. J Pharm Sci.

513   2015;104(8):2600-10. doi: 10.1002/jps.24518. PubMed PMID: 26036431.

514   10.   Gavze E, Shapiro M. Motion of inertial spheroidal particles in a shear flow near a

515   solid wall with special application to aerosol transport in microgravity. Journal of Fluid

516   Mechanics. 1998;371:59±79.

517   11.   Lee SY, Ferrari M, Decuzzi P. Shaping nano-/micro-particles for enhanced vascular

518   interaction in laminar flows. Nanotechnology. 2009;20 495101 (11pp).

519   12.   Gentile F, Chiappini C, Fine D, Bhavane RC, Peluccio MS, Cheng MM, et al. The

520   effect of shape on the margination dynamics of non-neutrally buoyant particles in

521   two-dimensional shear flows. J Biomech. 2008;41(10):2312-8. Epub 2008/06/24.

522   doi: S0021-9290(08)00150-4 [pii] 10.1016/j.jbiomech.2008.03.021. PubMed PMID:

523   18571181.

524   13.   Perera VS, Covarrubias G, Lorkowski M, Atukorale P, Rao A, Raghunathan S, et al.

525   One-pot synthesis of nanochain particles for targeting brain tumors. Nanoscale.

526   2017;9(27):9659-67. doi: 10.1039/c7nr02370g. PubMed PMID: 28675230; PubMed

527   Central PMCID: PMC5557407.

528   14.   Peiris PM, Abramowski A, Mcginnity J, Doolittle E, Toy R, Gopalakrishnan R, et al.

529   Treatment of invasive brain tumors using a chain-like nanoparticle. Cancer

530   Research. 2015;75(7):1356-65.

531   15.   Saul JM, Annapragada AV, Bellamkonda RV. A dual-ligand approach for enhancing

532   targeting   selectivity   of   therapeutic   nanocarriers.   J   Control   Release.

533   2006;114(3):277-87. Epub 2006/08/15. doi: S0168-3659(06)00250-1 [pii]

534   10.1016/j.jconrel.2006.05.028. PubMed PMID: 16904220.

535   16. Gay LJ, Felding-Habermann B. Contribution of platelets to tumour metastasis. Nat

536   Rev Cancer. 2011;11(2):123-34. Epub 2011/01/25. doi: nrc3004 [pii]

537   10.1038/nrc3004. PubMed PMID: 21258396.

538   17. Fukumura D, Jain RK. Tumor microenvironment abnormalities: causes,

539   consequences, and strategies to normalize. Journal of cellular biochemistry.

540   2007;101(4):937-49. PubMed PMID: 17171643.

541   18. Hobbs SK, Monsky WL, Yuan F, Roberts WG, Griffith L, Torchilin VP, et al.

542   Regulation of transport pathways in tumor vessels: role of tumor type and

543   microenvironment. Proc Natl Acad Sci U S A. 1998;95(8):4607-12. PubMed PMID:

544   9539785; PubMed Central PMCID: PMC22537.

545   19. Karathanasis E, Suryanarayanan S, Balusu SR, McNeeley K, Sechopoulos I,

546   Karellas A, et al. Imaging nanoprobe for prediction of outcome of nanoparticle

547   chemotherapy by using mammography. Radiology. 2009;250(2):398-406. PubMed

548   PMID: 19188313.

549   20. Huebschman ML, Lane NL, Liu H, Sarode VR, Devlin JL, Frenkel EP. Molecular

550   heterogeneity in adjacent cells in triple-negative breast cancer. Breast cancer.

551   2015;7:231-7. doi: 10.2147/BCTT.S87041. PubMed PMID: 26316815; PubMed

552   Central PMCID: PMC4540115.

553   21. Norton KA, Popel AS, Pandey NB. Heterogeneity of chemokine cell-surface receptor

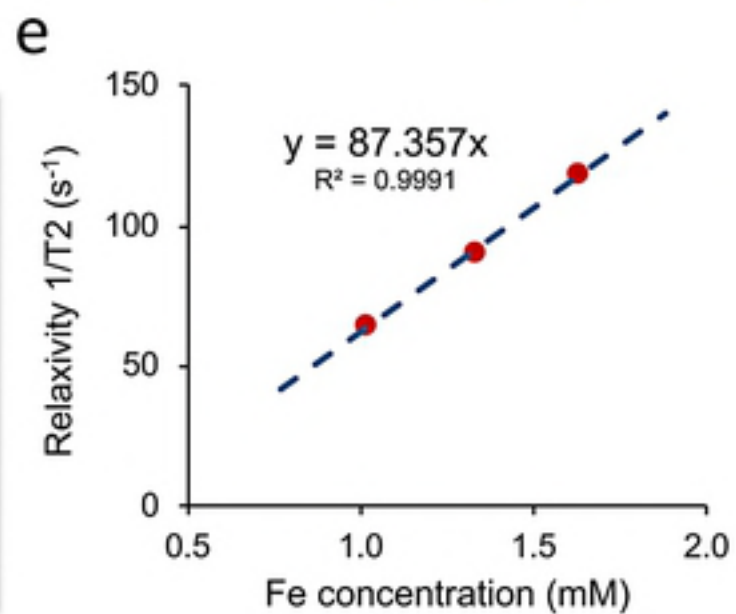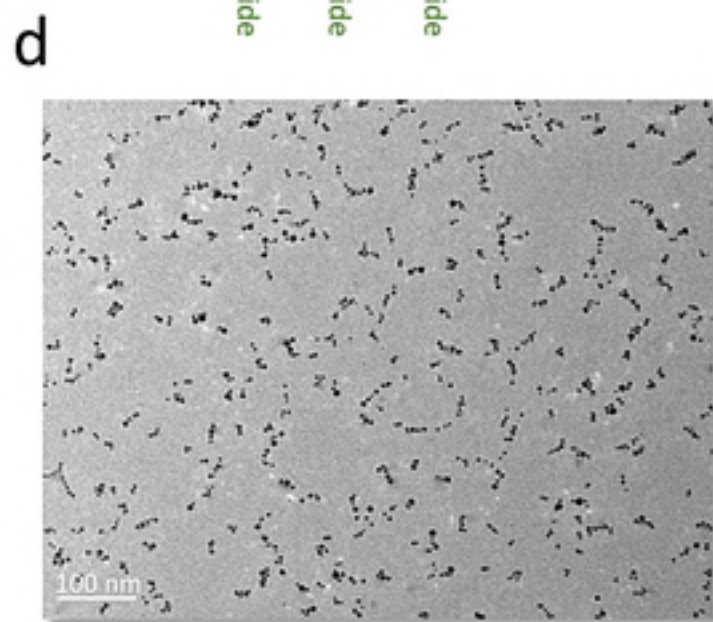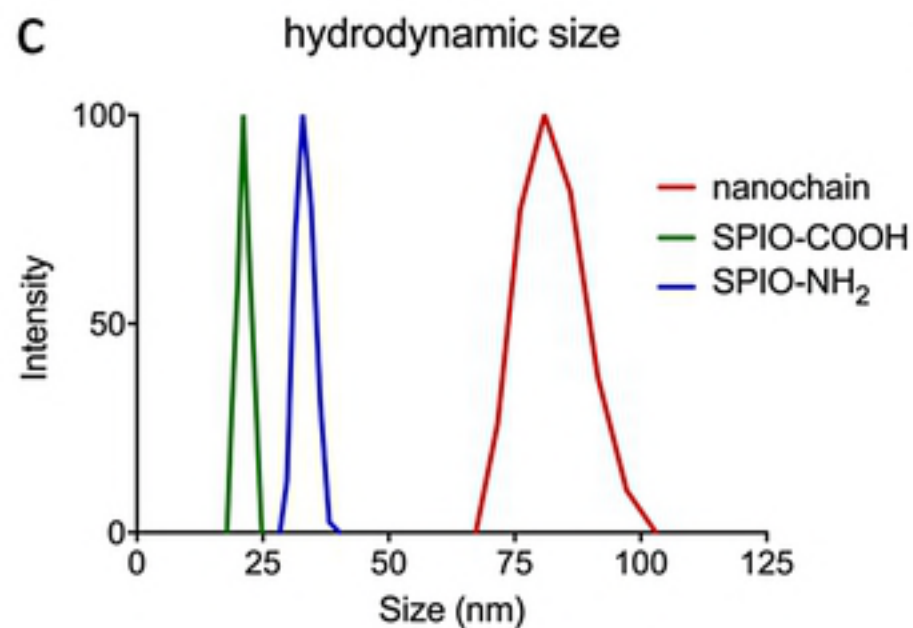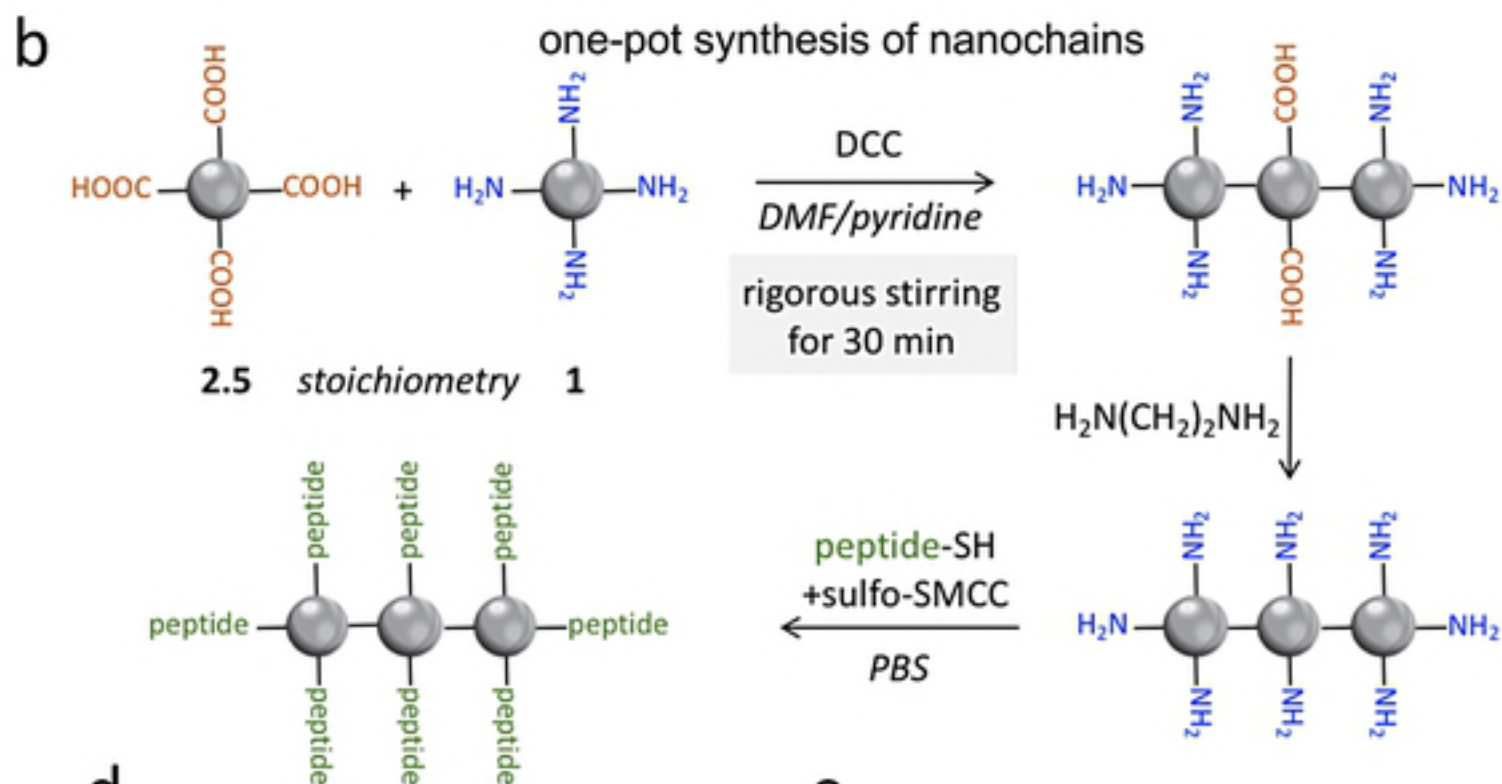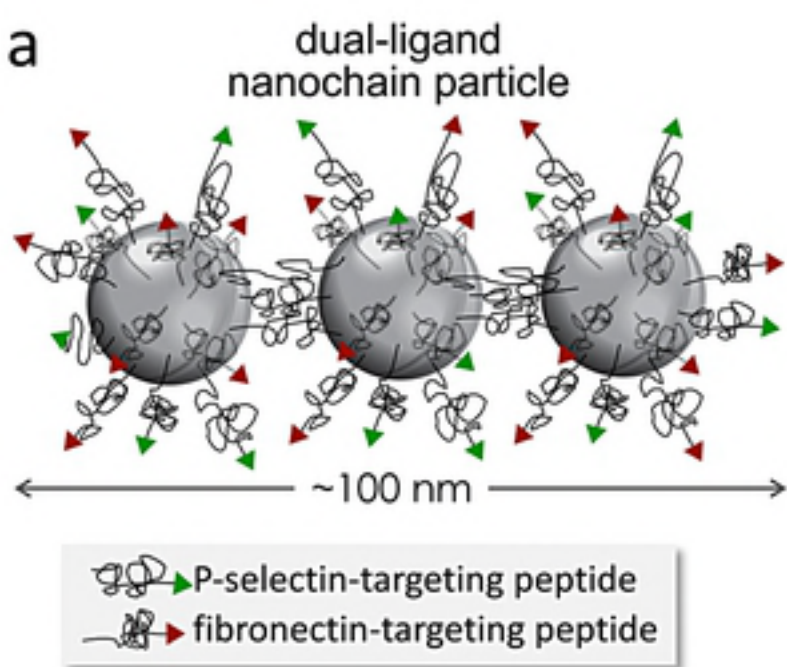554   expression in triple-negative breast cancer. American journal of cancer research.

555   2015;5(4):1295-307. PubMed PMID: 26101698; PubMed Central PMCID:

556   PMC4473311.

557   22. Martinez-Revollar G, Garay E, Martin-Tapia D, Nava P, Huerta M, Lopez-Bayghen

558   E, et al. Heterogeneity between triple negative breast cancer cells due to differential

559   activation of Wnt and PI3K/AKT pathways. Exp Cell Res. 2015;339(1):67-80. doi:

560   10.1016/j.yexcr.2015.10.006. PubMed PMID: 26453937.

561   23. Schnell O, Krebs B, Carlsen J, Miederer I, Goetz C, Goldbrunner RH, et al. Imaging

562   of integrin alpha(v)beta(3) expression in patients with malignant glioma by [18F]

563   Galacto-RGD positron emission tomography. Neuro-oncology. 2009;11(6):861-70.

564   doi: 10.1215/15228517-2009-024. PubMed PMID: 19401596; PubMed Central

565   PMCID: PMC2802406.

566   24. Reardon DA, Nabors LB, Stupp R, Mikkelsen T. Cilengitide: an integrin-targeting

567   arginine-glycine-aspartic acid peptide with promising activity for glioblastoma

568   multiforme. Expert opinion on investigational drugs. 2008;17(8):1225-35. doi:

569   10.1517/13543784.17.8.1225. PubMed PMID: 18616418; PubMed Central PMCID:

570   PMC2832832.

571   25. Danhier F, Vroman B, Lecouturier N, Crokart N, Pourcelle V, Freichels H, et al.

572   Targeting of tumor endothelium by RGD-grafted PLGA-nanoparticles loaded with

573   paclitaxel. J Control Release. 2009;140(2):166-73. Epub 2009/08/25. doi: S0168-

574   3659(09)00547-1 [pii]

575   10.1016/j.jconrel.2009.08.011. PubMed PMID: 19699245.

576   26. Reddy GR, Bhojani MS, McConville P, Moody J, Moffat BA, Hall DE, et al. Vascular

577   targeted nanoparticles for imaging and treatment of brain tumors. Clin Cancer Res.

578   2006;12(22):6677-86. doi: 10.1158/1078-0432.CCR-06-0946. PubMed PMID:

579   17121886.

580   27. Shamay Y, Elkabets M, Li H, Shah J, Brook S, Wang F, et al. P-selectin is a

581   nanotherapeutic delivery target in the tumor microenvironment. Science translational

582   medicine. 2016;8(345):345ra87. doi: 10.1126/scitranslmed.aaf7374. PubMed PMID:

583   27358497; PubMed Central PMCID: PMC5064151.

584   28. Laubli H, Borsig L. Selectins promote tumor metastasis. Seminars in cancer biology.

585   2010;20(3):169-77. doi: 10.1016/j.semcancer.2010.04.005. PubMed PMID:

586   20452433.

587   29. Kim YJ, Borsig L, Han HL, Varki NM, Varki A. Distinct selectin ligands on colon

588   carcinoma mucins can mediate pathological interactions among platelets,

589   leukocytes, and endothelium. Am J Pathol. 1999;155(2):461-72. doi:

590   10.1016/S0002-9440(10)65142-5. PubMed PMID: 10433939; PubMed Central

591   PMCID: PMC1866847.

592   30. Ludwig RJ, Boehme B, Podda M, Henschler R, Jager E, Tandi C, et al. Endothelial

593   P-selectin as a target of heparin action in experimental melanoma lung metastasis.

594   Cancer Res. 2004;64(8):2743-50. PubMed PMID: 15087389.

595   31. Nierodzik ML, Karpatkin S. Thrombin induces tumor growth, metastasis, and

596   angiogenesis: Evidence for a thrombin-regulated dormant tumor phenotype. Cancer

597   Cell. 2006;10(5):355-62. doi: 10.1016/j.ccr.2006.10.002. PubMed PMID: 17097558.

598   32. Borsig L, Wong R, Feramisco J, Nadeau DR, Varki NM, Varki A. Heparin and cancer

599   revisited: mechanistic connections involving platelets, P-selectin, carcinoma mucins,

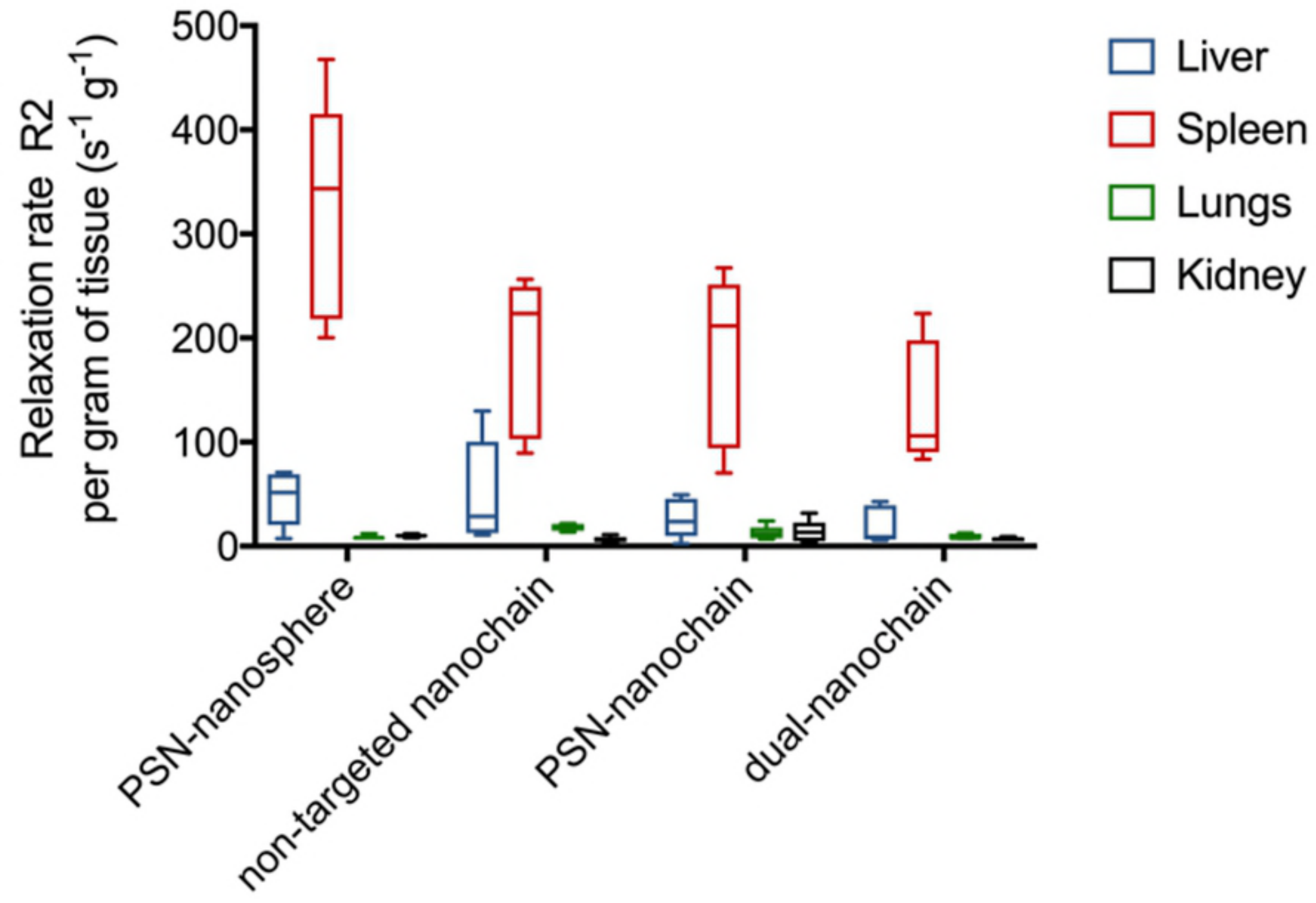600   and tumor metastasis. Proc Natl Acad Sci U S A. 2001;98(6):3352-7. doi:

601   10.1073/pnas.061615598. PubMed PMID: 11248082; PubMed Central PMCID:

602   PMC30657.

603   33. Mousa SA, Petersen LJ. Anti-cancer properties of low-molecular-weight heparin:

604   preclinical evidence. Thromb Haemost. 2009;102(2):258-67. doi: 10.1160/TH08-12-

605   0832. PubMed PMID: 19652876.

606   34. Serres E, Debarbieux F, Stanchi F, Maggiorella L, Grall D, Turchi L, et al. Fibronectin

607   expression in glioblastomas promotes cell cohesion, collective invasion of basement

608   membrane in vitro and orthotopic tumor growth in mice. Oncogene.

609   2014;33(26):3451-62. doi: 10.1038/onc.2013.305. PubMed PMID: 23912459.

610   35. Ohnishi T, Hiraga S, Izumoto S, Matsumura H, Kanemura Y, Arita N, et al. Role of

611   fibronectin-stimulated tumor cell migration in glioma invasion in vivo: clinical

612   significance of fibronectin and fibronectin receptor expressed in human glioma

613   tissues. Clin Exp Metastasis. 1998;16(8):729-41. PubMed PMID: 10211986.

614   36. Neri D, Bicknell R. Tumour vascular targeting. Nat Rev Cancer. 2005;5(6):436-46.

615   doi: 10.1038/nrc1627. PubMed PMID: 15928674.

616   37. Borsi L, Balza E, Bestagno M, Castellani P, Carnemolla B, Biro A, et al. Selective

617   targeting of tumoral vasculature: comparison of different formats of an antibody

618   (L19) to the ED-B domain of fibronectin. Int J Cancer. 2002;102(1):75-85. doi:

619   10.1002/ijc.10662. PubMed PMID: 12353237.

620   38. Peiris PM, Bauer L, Toy R, Tran E, Pansky J, Doolittle E, et al. Enhanced Delivery

621   of Chemotherapy to Tumors Using a Multicomponent Nanochain with Radio-

622   Frequency-Tunable Drug Release. ACS Nano. 2012;6(5):4157-68. Epub

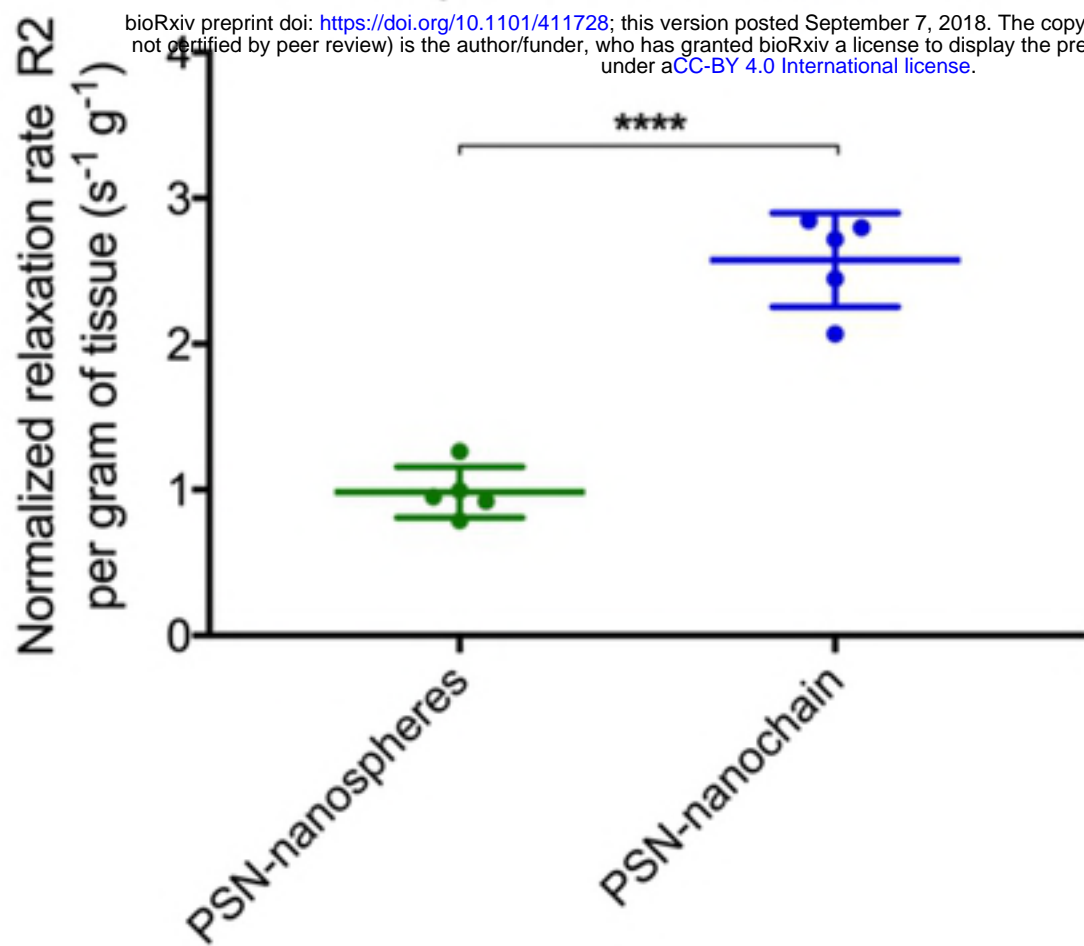623   2012/04/11. doi: 10.1021/nn300652p. PubMed PMID: 22486623.

624   39. Baumann BC, Kao GD, Mahmud A, Harada T, Swift J, Chapman C, et al. Enhancing

625   the efficacy of drug-loaded nanocarriers against brain tumors by targeted radiation

626   therapy. Oncotarget. 2013;4(1):64-79. doi: 10.18632/oncotarget.777. PubMed

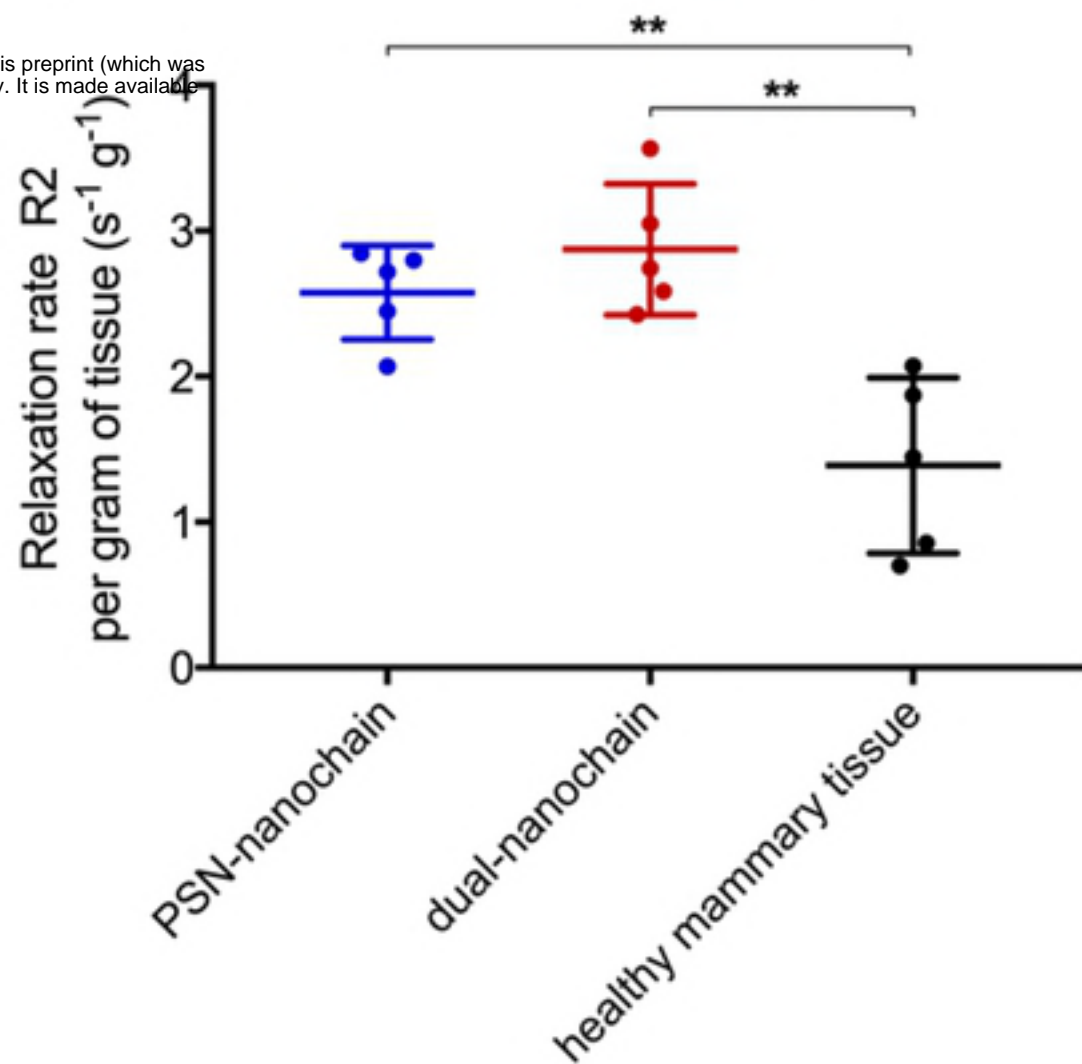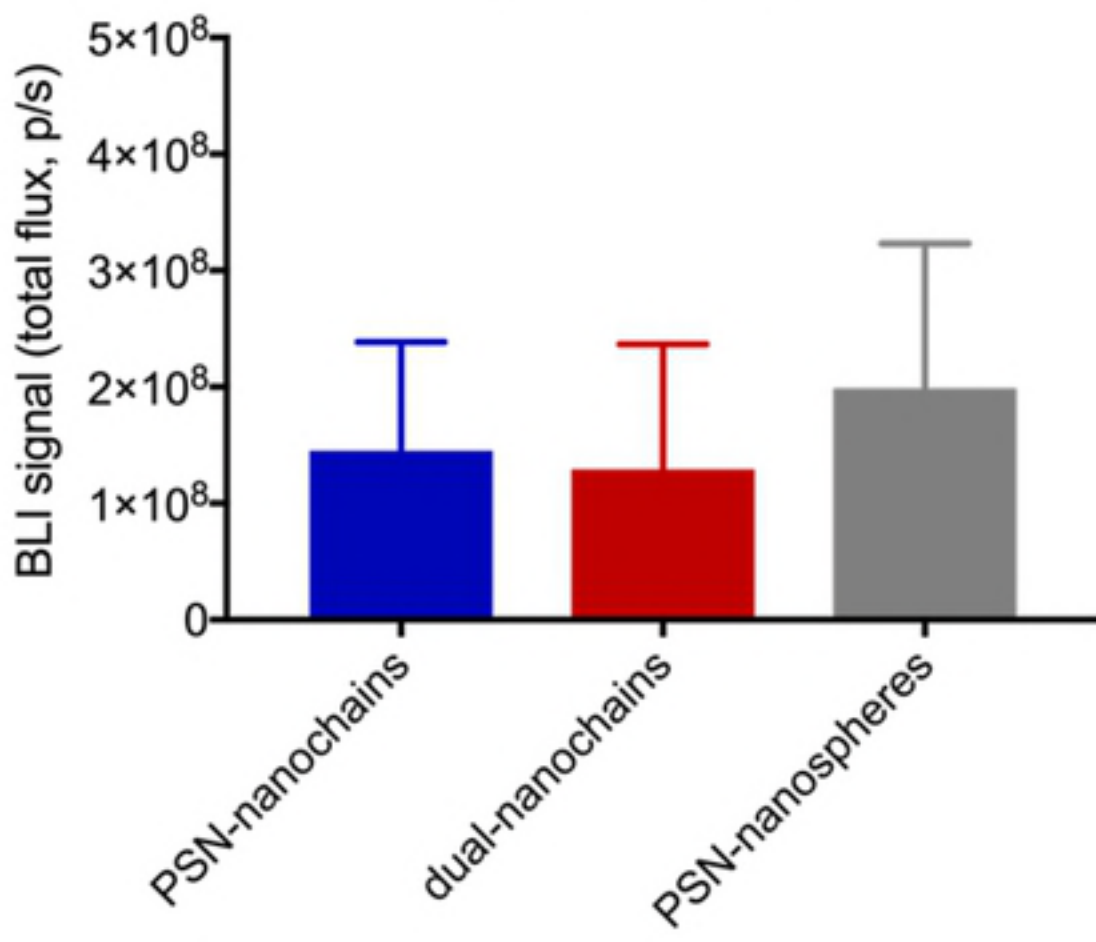627   PMID: 23296073; PubMed Central PMCID: PMCPMC3702208.

628

a dual-ligand nanochain particle

~100 nm

P-selectin-targeting peptide
fibronectin-targeting peptide

b one-pot synthesis of nanochains

HOOC—[●]—COOH + H₂N—[●]—NH₂ →(DCC / DMF/pyridine)→ nanochain intermediate

2.5   *stoichiometry*   1

rigorous stirring for 30 min

H₂N(CH₂)₂NH₂

peptide-SH + sulfo-SMCC / PBS

peptide-nanochain product

c hydrodynamic size

Intensity vs Size (nm)

— nanochain
— SPIO-COOH
— SPIO-NH₂

d

100 nm

e

$y = 87.357x$
$R^2 = 0.9991$

Relaxivity 1/T2 (s⁻¹) vs Fe concentration (mM)

Organic distribution

a

tumor targeting
nanospheres vs. nanochains

b

tumor targeting

c

tumor burden

d

targeting accuracy

a MRI in vivo

Normalized signal intensity

- pre-injection
- 3h post-injection

$*$

$**$

no contrast

4T1   D2.A1

b pre-injection   3 h post-injection

tumor   tumor

a   *serial tissue sections*

DAPI / CD31   100 μm

cancer cell / fibronectin   100 μm

cancer cell / P-selectin   100 μm
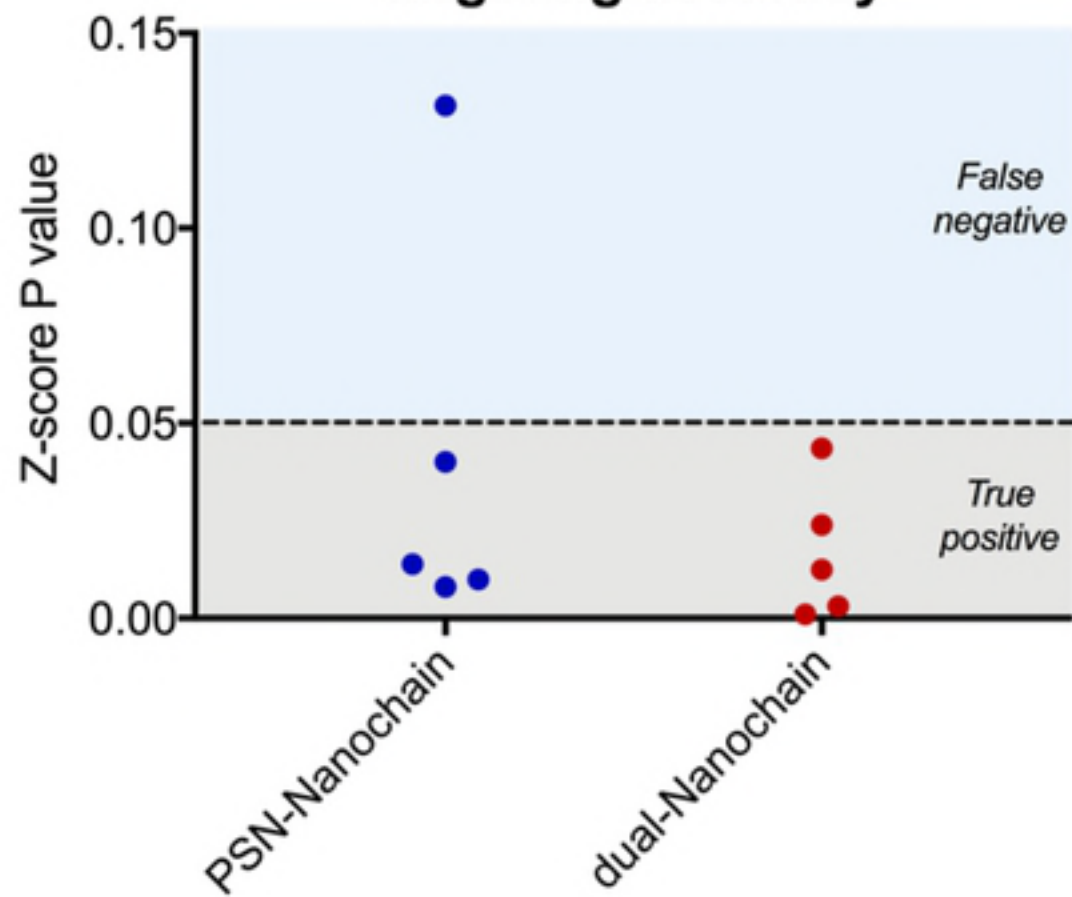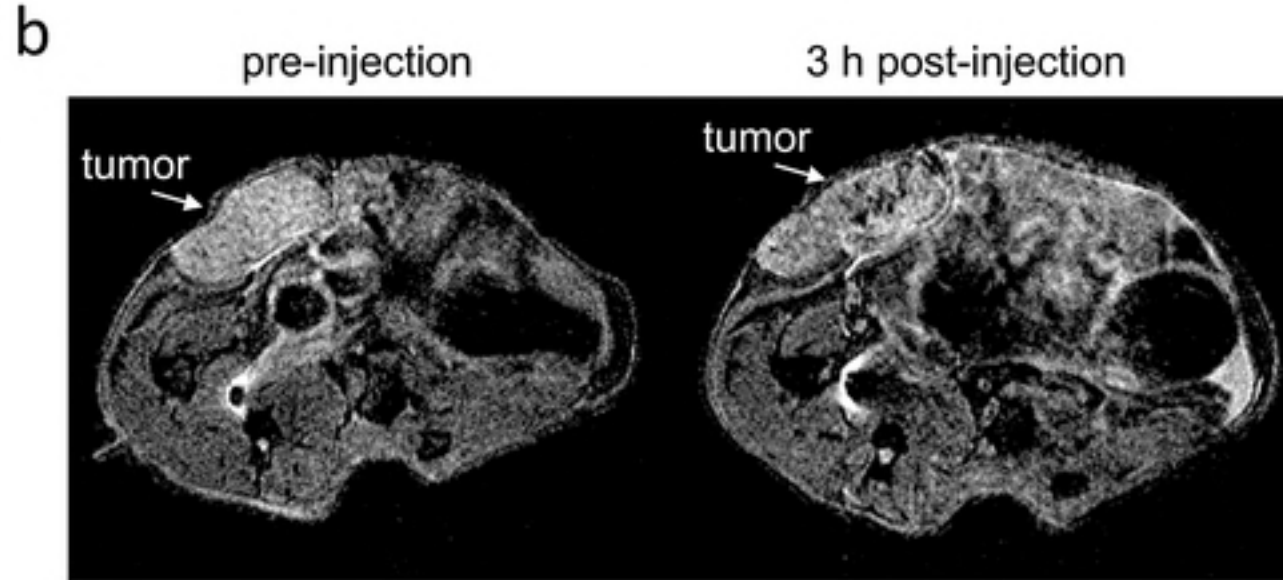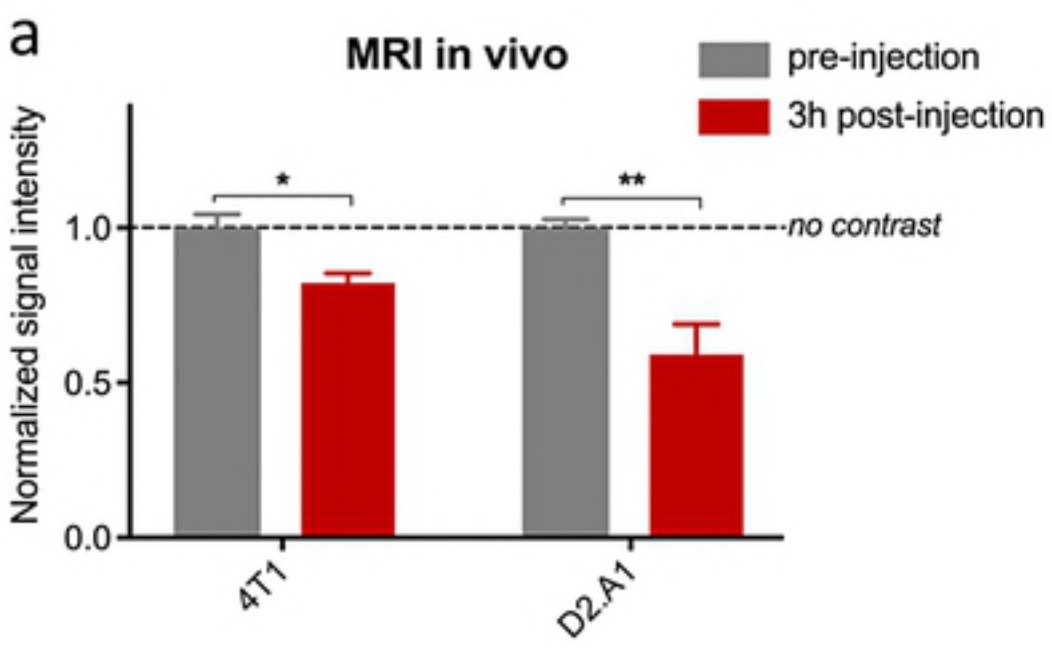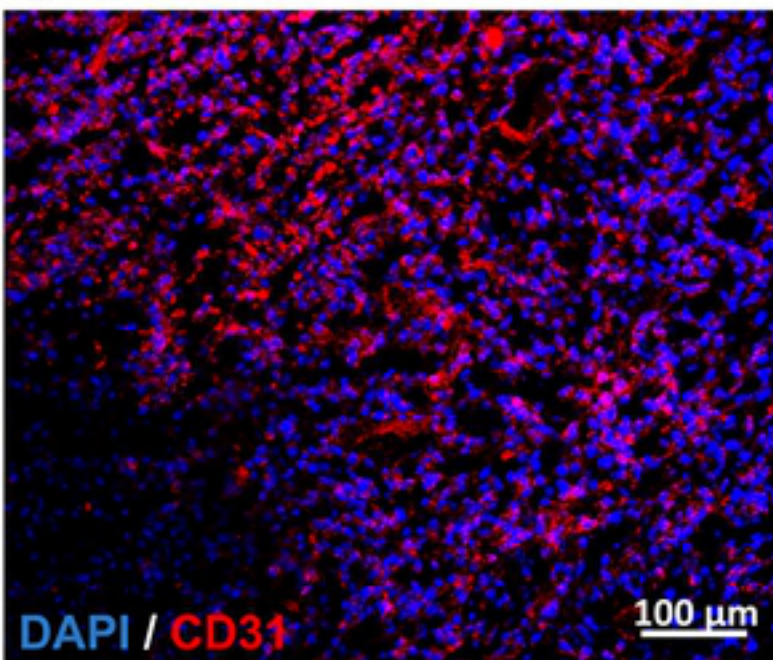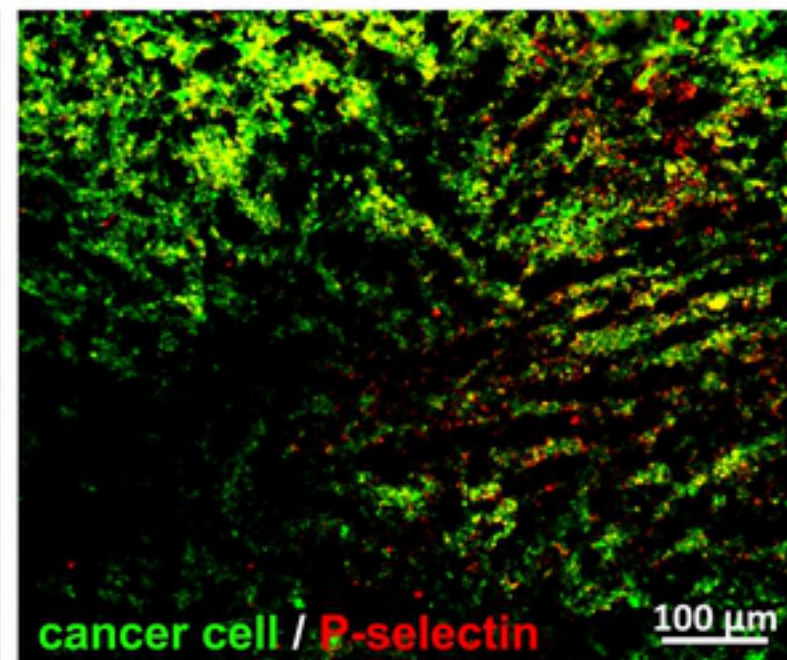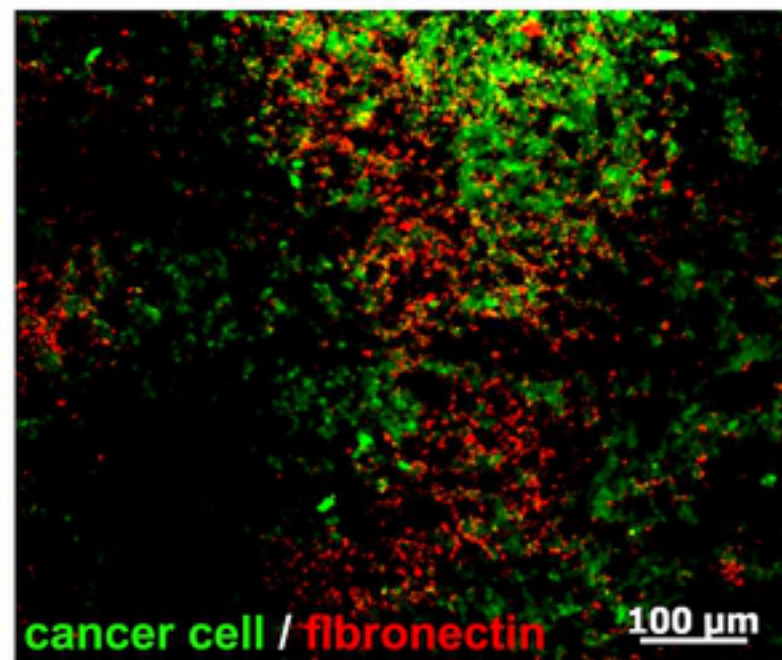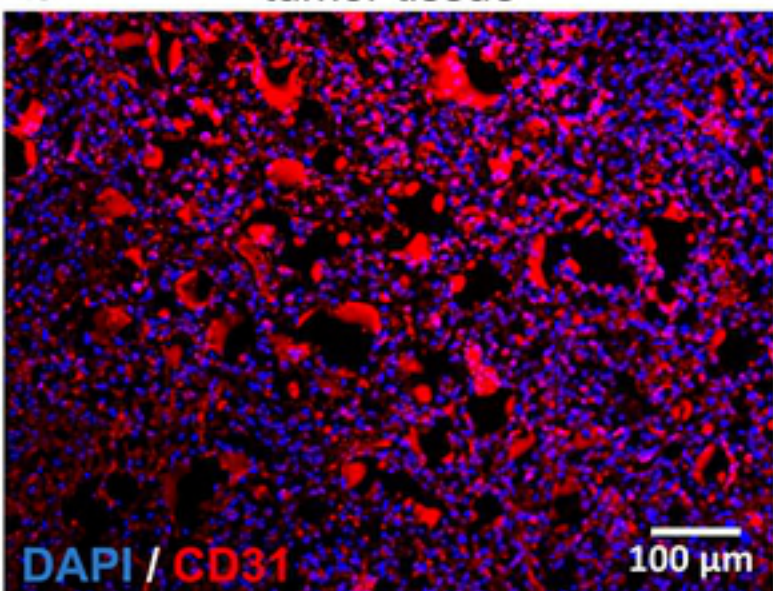
b   tumor tissue   *from same tumor tissue at high magnification*

DAPI / CD31   100 μm

Prussian Blue   20 μm

20 μm